An Organoid for Woven Bone

Anat Akiva^[1,3,4,5]*, Johanna Melke^[2,3], Sana Ansari[2,3,5], Nalan Liv[6], Robin van der Meijden[5,7], Merijn van Erp,[1,4] Feihu Zhao[2,3,8], Merula Stout[5], Wouter H. Nijhuis[9], Cilia de Heus[6], Claudia Muñiz Ortera[5], Job Fermie[6], Judith Klumperman[6], Keita ito[2,3], Nico Sommerdijk[3,4,5,7*], Sandra Hofmann[2,3]*

Affiliations:

1. Department of Cell Biology, Radboud Institute of Molecular Life Sciences, Radboud University Medical Center, Geert Grooteplein 6525 GA Nijmegen, The Netherlands

2. Orthopaedic Biomechanics, Department of Biomedical Engineering, Eindhoven University of Technology, PO Box 513, 5600 MB, Eindhoven, the Netherlands

3. Institute for Complex Molecular Systems (ICMS), Eindhoven University of Technology, PO Box 513, 5600 MB, Eindhoven, the Netherlands

4. Electron Microscopy Center, Radboud Institute of Molecular Life Sciences, Radboud University Medical Center, Geert Grooteplein 6525 GA Nijmegen, The Netherlands

5. Department of Chemical Engineering and Chemistry, Laboratory of Materials and Interface Chemistry PO Box 513, 5600 MB, Eindhoven, the Netherlands

6. Section Cell Biology, Center for Molecular Medicine, University Medical Center Utrecht, Utrecht, The Netherlands

7. Department of Biochemistry, Radboud Institute of Molecular Life Sciences, Radboud University Medical Center, Geert Grooteplein 6525 GA Nijmegen, The Netherlands

22 8. Zienkiewicz Centre for Computational Engineering, College of Engineering, Swansea
23 University, Swansea, SA1 8EN, United Kingdom.

24 9. Department of Orthopaedic Surgery, University Medical Centre Utrecht, Wilhelmina
25 Children's Hospital, The Netherlands.

26

27 ^equal contribution

28 Corresponding authors: anat.akiva@radboudumc.nl ; nico.sommerdijk@radboudumc.nl;
29 s.hofmann@tue.nl

30 **Stem cell-based organoids are promising as functional, self-organizing 3D *in vitro* models for**
31 **studying the physiology and pathology of various tissues[1]. Bone formation (osteogenesis) is a**
32 **complex process in which i) cellular differentiation and ii) the generation of a mineralized organic**
33 **matrix are synchronized to produce a hybrid hierarchical architecture. To study the molecular**
34 **mechanisms of osteogenesis in health and disease there is great need for organoids that capture**
35 **both processes in parallel[2], however, for human bone no such functional model system is yet**
36 **available[3].**

37 **Here, we report the *in vitro* differentiation of human bone marrow stromal cells into a functional**
38 **3D self-organizing co-culture of osteoblasts and osteocytes, creating an organoid for early stage**
39 **bone (woven bone) formation. We demonstrate that the osteocytes form a network showing cell-**
40 **cell communication via the expression of sclerostin, embedded within the collagen matrix that is**
41 **formed by the osteoblasts and mineralized under biological control**.

42 Organoids have been defined as “in vitro 3D cellular clusters derived exclusively from embryonic
43 stem cells, induced pluripotent stem cells or primary tissue, capable of self-renewal and self-
44 organization, and exhibiting similar organ functionality as the tissue of origin”, where they may “rely

on artificial extracellular matrices (ECM) to facilitate their self-organization into structures that resemble native tissue architecture"[1]. In the case of bone, such a model system where mechanical and (bio)chemical signals can be applied in a dynamic environment, would be an important tool in the development of treatments for bone related human diseases such as osteoporosis and skeletal dysplasia such as osteogenesis imperfecta, and aid in the development of strategies for personalized bone regenerative medicine.

Realizing a 3D model with different interacting bone cell types is, however, still an enormous challenge. In particular the differentiation of *human* bone marrow-derived mesenchymal stromal cells (BMSCs) into osteocytes, which form 90-95% of the cellular fraction of bone tissue[4], has not yet been achieved *in vitro* and currently remains a critical step in the engineering of *in vitro* human bone models.

In vivo, osteocytes form through the differentiation of osteoblasts, after these become embedded in the extracellular matrix they produce[4,5]. Osteocytes are responsible for sensing the biophysical demands placed on the tissue and orchestrating the concomitant actions of osteoblasts and osteoclasts in the remodeling of bone[2], as well as for maintaining calcium and phosphate homeostasis. During the differentiation from osteoblasts to osteocytes, the cells grow long extensions called processes, by which they form a sensory network that translates mechanical cues into biochemical signals and through which they interact with other cells[2].

In vitro, osteoblast-based cell lines developed as models of osteocytes or osteocyte differentiation have not yet been shown to produce a fully developed mineralized collagen matrix[6], and hence are limited as 3D models for bone formation. So far, the full differentiation from MSCs to functional osteocytes has been demonstrated for mouse cells[7,8] but not yet for human cells. Recently, pre-osteocyte-like cells have been achieved from human primary cells[9,10], and co-cultures were generated from pre-prepared populations of osteoblasts and osteocytes[11], but the *in vitro* production of a bone-like mineralized matrix formed under biological control was not yet demonstrated. Also

70 missing is a demonstration of the production of sclerostin by osteocytes at the protein level, where
71 sclerostin is a key anti-anabolic molecule that interacts with osteoblasts to down-regulate ECM
72 formation. Hence, the creation of an organoid, as a model for developing bone, through the full
73 differentiation of human primary cells into a functional osteocyte network within a bone-like
74 mineralized matrix is still an outstanding challenge.

75 In the present work, primary human bone marrow stromal cells (hBMSC) were seeded on porous 3D
76 silk fibroin scaffolds[12] and subsequently cultured in osteogenic differentiation medium. The cells
77 were exposed to mechanical stimulation through fluid flow derived shear stress, by applying
78 continuous stirring in a specifically designed spinner-flask bioreactor (Supplementary Fig. 1)[13], while a
79 static system was used as control. Cells subjected to mechanical loading showed the production of a
80 mineralized extracellular matrix (ECM) - as assessed by micro-computed tomography (μCT) and
81 histological staining for collagen, glycosaminoglycans and minerals (Supplementary Fig. 2). Fourier-
82 Transformed Infrared (FTIR) spectroscopy indicated a matrix composition similar to that of
83 embryonic chicken bones (Supplementary Fig. 3)[14]. In contrast, no significant ECM production was
84 observed in the static system.

85 The differentiation from primary cells to osteoblasts and osteocytes was followed using
86 immunohistochemistry, visualizing the expression of specific biomarkers at the protein level for the
87 subsequent development to pre-osteoblasts, osteoblasts and osteocytes[2] (Fig. 1, Supplementary Fig.
88 4). The pre-osteoblastic stage was identified by the expression of transcription factors RUNX2 (CBFA-
89 1) and osterix (OSX, SP7) (Fig. 1 a-b, Supplementary Fig. 4). The next stage in the differentiation, the
90 formation of osteoblasts, was heralded by the detection of osteoblast-specific markers, where
91 alkaline phosphatase (ALP) was detected at the cell surfaces, and osteocalcin (BGLAP), osteopontin
92 (BSP1) and osteonectin (SPARC) localized in the cellular environment (Fig. 1 c-f, Supplementary Fig.
93 4). Finally, the differentiation into osteocytes was indicated by the expression of dentin matrix
94 protein1 (DMP1), podoplanin (E11) and sclerostin (Fig. 1 g-i, Supplementary Fig. 4). DMP1 is a marker

95 for the early stages of osteocyte formation, coinciding with the embedding of the osteoblasts in the
96 collagenous matrix. Podoplanin marks the osteocyte embedded in the non-mineralized matrix stage
97 and has been suggested to regulate process formation[4]. Sclerostin indicates the maturation of the
98 osteocytes and their ability to perform their signaling function in the bone regulatory process[2,15]. We
99 note that the rate of osteocyte differentiation depended on the glucose concentration in the
100 medium, as indicated by the detection of sclerostin after ~4 weeks for 5.55 mM glucose (Fig. 1 i) and
101 ~ 8 weeks for 25 mM glucose (Fig. 1 k).

102 Fluorescence microscopy using calcein staining showed the co-localization of sclerostin and mineral
103 in large domains with dimensions of hundreds of micrometers, indicating the embedding of the
104 osteocytes in a mineralized organic matrix (Fig. 1 k). Indeed, combined staining with calcein (mineral)
105 and CNA35 (collagen) revealed the presence of sub-millimeter sized mineralized collagen domains
106 (Fig. 1 l) throughout the entire scaffold, co-existing with non-mineralized domains osteoblast markers
107 were also still observed (Supplementary Fig. 5). This implies that this co-culture presents different
108 stages of osteogenic cell differentiation and maturation in which osteocytes had formed that
109 organized themselves with the mineralized matrix also produced by the system.

110 Fluorescence microscopy further confirmed osteocyte formation showing the development of cell
111 processes, and the formation of an interconnected network (Fig. 2 a). Additionally, three dimensional
112 focused ion beam/scanning electron microscopy (3D FIB/SEM) showed that the cells form a relatively
113 dense 3D network with significant variation in their morphologies, as well as in the number, lengths
114 and connectivity of their processes (Fig. 2 b-e, Supplementary table 1 and 2). We note that our
115 osteocytes most often show flattened morphologies, which differ from those in text books with
116 generally spherical or oblate bodies and long homogeneous protrusions but are similar to osteocyte
117 morphologies observed in different bone types, including rat tibia,[16] human femur[17] and mouse
118 woven bone[18].

119 Cells showed both connected and unconnected processes, with connections to 1-7 neighboring cells
120 (Fig 2 f, Supplementary Fig. 7 and table 2). The network had a density of 750,000 cells.mm^{-3}, which is
121 higher than observed for mature osteocytes in cortical bone (20,000-80,000 cells.mm^{-3})[5], but in line
122 with numbers found for woven bone such as in embryonic chicken tibia (500,000-700,000 cells.mm^{-}
123 ^{3})[19]. Image analysis (Supplementary Fig. 11) showed that for the different cells the number of
124 processes per unit surface area ranged between 0.05 - 0.23 µm^{-2} (Supplementary Table 3), in line
125 with reported for mouse osteocytes (0.08 – 0.09 µm^{-2})[20]. The functionality of the processes was
126 indicated not only by their connection to neighboring cells (Fig. 2 g-h), but also by their co-
127 localization with connexin43, a protein essential for gap junction communication (Fig. 2 i)[2]. The
128 observed variation in osteocyte morphology, together with the variation in the number of cell
129 processes per surface area reflects the different stages of development and maturation, as expected
130 in a differentiating osteogenic co-culture.

131 To evaluate the physiological relevance of our co-culture model system, we also analyzed its
132 capability to reproduce the bone extracellular matrix. FIB/SEM volume imaging with 3D
133 reconstruction showed that the osteocytes were fully embedded in their ECM (Fig. 3 a; Video 1). The
134 produced collagen matrix enveloped the cells, but showed a low degree of long range order (Fig. 3 b),
135 as known for woven bone[18,21], and in line with what was described for collagen layers containing
136 osteocytes.[22] The extracellular deposition of non-collagenous proteins (NCPs) was evidenced by
137 immunohistochemical analysis, showing the presence of osteocalcin, osteopontin, and DMP1 and
138 their co-localization with collagen (Fig. 3 c-d, Supplementary Fig. 8).

139 Whereas µCT (Supplementary Fig. 2), FTIR (Supplementary Fig. 3), histochemistry (Supplementary
140 Fig. 2), and fluorescence microscopy (Fig. 1 k) all indicated the mineralization of the organic matrix,
141 none of these methods can provide the spatial resolution to demonstrate whether the mineral
142 crystals are indeed, as in bone, co-assembled with the collagen fibrils[23], and not just the result of
143 uncontrolled precipitation[24]. We therefore applied a multiscale imaging approach to verify that

144 matrix mineralization indeed occurred under biological control. Raman micro-spectroscopy of the
145 extracellular matrix showed the spectral signature of developing bone (Fig. 3 f) and confirmed the co-
146 localization of the mineral with the collagen (Supplementary Fig. 9). Spectral analysis further
147 confirmed that the mineral/matrix ratio (a key parameter for bone development, determined from
148 the PO_4 ν_4 / Amide III vibrations intensity ratio [25]) in the co-culture was indeed in the range found for
149 developing bone (Fig. 3 g)[26].

150 At higher resolution (voxel size 10x10x20 nm^3), 3D FIB/SEM with back scatter detection revealed thin
151 collagen fibrils (diameters 50-80 nm) with varying degrees of mineralization as also commonly
152 observed in the early stages of bone development[27] (Fig. 3 i, video-2, supplementary Fig. 10).
153 Applying a heat map presentation showed the coexistence of non-mineralized fibrils (blue) alongside
154 a mineralized population (green-red range). Additionally, transmission electron microscopy (TEM)
155 showed mineralized single fibrils,[7] indicating that the collagen matrix was indeed mineralized under
156 biological control (Fig. 3 j)[28]**.** Nevertheless, in some areas also larger mineral precipitates were
157 observed (Supplementary Fig. 10 c, orange) (Video-2), possibly due to local non-biologically
158 controlled precipitation of calcium phosphate.

159 Woven bone is the first form of mammalian bone deposited during embryonic development and
160 fracture, before being replaced by other bone types.[21] Hence, in situations in which rapid formation
161 is a prime concern, and where osteoclasts and bone remodeling do not yet play a role. Our results
162 show the formation of a bone organoid consisting of a self-organized co-culture of osteoblasts and
163 osteocytes representing a functional model for woven bone. We demonstrate the functionality of the
164 organoid by showing that the ECM formed by the osteoblasts is mineralized under biological control,
165 and that the mature osteocytes self-organize into a network within the mineralized matrix where
166 they express sclerostin and connexin43 at the protein level.

167 Interestingly, the production of sclerostin did not prohibit ECM formation throughout the organoid,
168 suggesting that the down regulation of this process is a local effect. This may be explained by

assuming the most mature osteocytes are in the center of the osteocyte domains, which would lead to a gradient of sclerostin decreasing towards the periphery of the network, only affecting the activity of the osteoblasts closest to the osteocyte domain.

The use of silk fibroin as a scaffold material rather than the frequently used collagen scaffolds, permits to differentiate between the supplied and the newly formed matrix material, and study the quality of the collagen matrix as function of external stimuli (mechanical load, therapeutics) or genetic diseases (e.g. osteogenesis imperfecta). The application of mechanical stimulation during the development of our stem cell based co-culture proved crucial for the osteogenic differentiation, and underlines the importance of the integration of self-organizing stem cell based strategies with environmental control in microfluidic systems in the recent organoid-on-a-chip approaches.[29]

Acknowledgments: We would like to thank like Lia Addadi and Steve Weiner for providing the zebrafish and embryonic chicken data, and Carlijn Bouten for providing CNA35 collagen probe. We also thank Deniz Daviran for her help in preparing the figures. AA was supported by the Marie Curie Individual Fellowship (H2020-MSCA-IF-2017-794296-SUPERMIN), by the Netherlands Organization for Scientific Research (NWO) through an ECHO grant to NS, and by the National Postdoctoral Award Program for Advancing Women in Science - the Weizmann Institute of Science, Israel. NS, RvdM and MvE were supported by the European Research Council (ERC) Advanced Investigator grant (H2020-ERC-2017-ADV-788982-COLMIN) to NS, SA was supported by the Ministry of Education, Culture and Science (Gravitation Program 024.003.013). NL was supported by the Netherlands Organization for Scientific Research (NWO) through a ZonMW-TOP grant to JK. JM, FZ and SH were supported by the ERC Starting grant (FP7-ERC-2013-StG-336043-REMOTE) to SH.

Author Contributions: AA, KI, NS, SH designed the project and wrote the paper. AA, JM, SA were responsible for 3D cell culture, light and fluorescent imaging and analyzed the data. NL, JF, CdeH and JK prepared samples for EM and took EM images. RvdM, AA and NS acquired and analyzed the

spectroscopic data. MS, CMO and AA performed the FIB/SEM reconstruction and segmentation. CMO, FZ, RvdM, AA, NS, MvE and SH analyzed the connectivity map of the osteocyte network. WHN provided the bone reference sample. All authors read the paper and gave their comments.

Competing Interests statement:

The authors declare no competing interests

Data availability statements:

The datasets generated during and/or analysed during the current study are available from the corresponding author on reasonable request

Code availability:

Computer codes are available at: https://filesender.surf.nl/?s=download&token=e5f72e20-2240-4f58-abeb-3ecbeaab54f2

209 **Materials and methods:**

210 **Materials:**

211 Dulbecco's modified Eagle medium (DMEM high glucose Cat. No. 41966 and low glucose Cat. No.
212 31885) and antibiotic/antimycotic (Anti-Anti) were from Life Technologies (Bleiswijk, The
213 Netherlands). Citrate buffer was from Thermo Fisher Scientific (Breda, The Netherlands). Methanol
214 was from Merck (Schiphol-Rijk, The Netherlands). Trypsin-EDTA (0.25%) was from Lonza (Breda, The
215 Netherlands). Fetal bovine serum (FBS) was from PAA Laboratories (Cat. No A15-151, Cölbe,
216 Germany). 10-nm Au particles conjugated to Protein-A were from CMC, UMC Utrecht (Utrecht, The
217 Netherlands). BSA-c was from Aurion (Wageningen, The Netherlands). Silkworm cocoons from
218 Bombyx mori L. were purchased from Tajima Shoji Co., LTD. (Yokohama, Japan). All other substances
219 were of analytical or pharmaceutical grade and obtained from Sigma Aldrich (Zwijndrecht, The
220 Netherlands). The reference human bone sample used for Raman micro-spectrometry was waste
221 material from a surgical procedure on a fractured left tibia of a 10-year-old female. According to the
222 Central Committee on Research involving Human Subjects (CCMO), this type of study does not
223 require approval from an ethics committee in the Netherlands (see
224 https://english.ccmo.nl/investigators/legal-framework-for-medical-scientific-research/your-research-
225 is-it-subject-to-the-wmo-or-not). For information on the embryonic chicken bone and zebrafish bone
226 we refer to references 14 (Kerschnitzky et al.) and 26 (Akiva et al.), respectively.

227

228 **Scaffold fabrication:**

229 Silk fibroin scaffolds were produced as previously described[30]. Briefly, Bombyx mori L. silkworm
230 cocoons were degummed by boiling in 0.2M Na_2CO_3 twice for 1 h. The dried silk was dissolved in 9 M
231 LiBr and dialyzed against ultra-pure water (UPW) for 36 h using SnakeSkin Dialysis Tubing (molecular
232 weight cutoff: 3.5 K; Thermo Fisher Scientific, Breda, The Netherlands). Dialyzed silk fibroin solution
233 was frozen at -80°C and lyophilized (Freezone 2.5, Labconco, Kansas City, MO, USA) for 4 days, then
234 dissolved in hexafluoro-2-propanol, resulting in a 17% (w/v) solution. 1 ml of dissolved silk fibroin

235 was added to 2.5 g NaCl with a granule diameter of 250–300 µm and was allowed to air dry for 3
236 days. Silk-salt blocks were immersed in 90% MeOH for 30 min to induce β-sheet formation[31]. NaCl
237 was extracted from dried blocks in UPW for 2 days. Scaffolds were cut into disks of 5 mm in diameter
238 and 3 mm in height and autoclaved in PBS at 121°C for 20 min.
239
240 **Cell culture:**
241 Cells were isolated from unprocessed, fresh, human bone marrow (Lonza, Walkersville, MD, USA, cat.
242 No #1M-125) of one male donor (healthy, non-smoker). hBMSC isolation and characterization was
243 performed as previously described and passaged up to passage 4[30]. Pre-wetted scaffolds were
244 seeded with 1 million cells each in 20 µL control medium (DMEM, 10% FBS, 1% Anti-Anti) and
245 incubated for 90 min at 37° C. The cell-loaded scaffolds were transferred to custom-made spinner
246 flask bioreactors (n = 4 per bioreactor, Supplementary Fig. 1). Each bioreactor contained a magnetic
247 stir bar and was placed on a magnetic stirrer (RTv5, IKA, Germany) in an incubator (37° C, 5% CO_2).
248 Each bioreactor was filled with 5 mL osteogenic medium (control medium, 50 µg/mL ascorbic-acid-2-
249 phosphate, 100 nM dexamethasone, 10 mM β-glycerophosphate) and medium was changed 3 times
250 a week.
251
252 **Micro-computed tomography imaging (µCT):**
253 µCT measurements and analysis were performed on a µCT100 imaging system (Scanco Medical,
254 Brüttisellen, Switzerland). Scanning of the co-culture samples within the bioreactor was performed at
255 an isotropic nominal resolution of 17.2 µm, energy level was set to 45 kVp, intensity to 200 µA, 300
256 ms integration time and two-fold frame averaging. A constrained Gaussian filter was applied to
257 reduce part of the noise. Filter support was set to 1.0 and filter width sigma to 0.8 voxel. Filtered
258 grayscale images were segmented at a global threshold of 23% of the maximal grayscale value to
259 separate the mineralized tissue from the background and binarize the image. Unconnected objects
260 smaller than 50 voxels were removed and neglected for further analysis. Quantitative

261 morphometrical analysis was performed to assess mineralized ECM volume within the entire scaffold
262 volume using direct microstructural bone analysis as previously described for human bone
263 biopsies[32,33].
264
265 **Histological sections:**
266 Co-cultures were fixed in 10% neutral buffered formalin (24 h at 4° C), dehydrated in serial ethanol
267 solutions (50%, 70%, 90%, 96%, 100%, 100%, 100%), embedded in paraffin, cut into 6 µm thick
268 sections and mounted on Poly-L-Lysine coated microscope slides. Paraffin sections were dewaxed
269 with xylene and rehydrated to water through graded ethanol solutions.
270 *Brightfield imaging*:
271 Sections were stained with Alizarin Red to identify mineralization (2%, Sigma-Aldrich), Picrosirius Red
272 (0.1%, Sigma-Aldrich) to identify collagen, Alcian blue (1%, Sigma-Aldrich) to identify
273 Glycosaminoglycan (GAGs). Sections were imaged using Zeiss Axio Observer Z1 microscope.
274 *Immunohistochemistry:*
275 Antigen retrieval in pH 6 citrate buffer at 95° C was performed for 20 min. Sections were washed
276 three times in PBS. Non-specific antibody binding was blocked with 5% serum (v/v) from the host of
277 the secondary AB and 1% bovine serum albumin (w/v) in PBS (blocking buffer) for 1 h. Sections were
278 then incubated overnight at 4° C with primary antibodies in blocking buffer. The sections were rinsed
279 with PBS four times for 5 min and incubated for 1 h with secondary antibodies in blocking buffer and
280 at times with calcein solution (1 µg/mL, C0875 Sigma-Aldrich). All used antibodies and dyes are listed
281 in Table 1. Nuclei were stained with DAPI for 5 min, after which sections were again washed three
282 times with PBS and mounted on microscope glass slides with Mowiol. Cytoplasm was stained with
283 FM 4-64 (Molecular Probes cat#T3166) for 1 minute and followed by washing the sections three
284 times with PBS. Except for primary antibody incubation, all incubation steps were performed at room
285 temperature. Sections were imaged either by Zeiss Axiovert 200M microscope (large field of view) or

286 by Leica TCS SP5X (x63, high magnification images). Images were post processed (brightness,

287 contrast, channel merging and crop) using Fiji software.

288 Table 1. List of all antibodies and dyes used.

Antigen	Source	Cat. No	Label	Species	Dilution/concentration
ALP	ThermoFisher	MA5-17030	-	Mouse	1:200
Calcein Green	Sigma	C0875	-	-	1 µg/ml
CNA35-mCherry	Homemade[34]	-	mCherry	-	1 µM
Collagen1	Abcam	ab34710	-	Rabbit	1:250
Connexin 43	Sigma	C6219	-	Rabbit	1:500
DAPI	Sigma	D9542	-	-	0.1 µg/ml
DMP1	biorbyt	orb247330	-	Rabbit	1:400
FM 4-64	Molecular Probes	T3166	-	-	5 µg/ml
Osteocalcin	Abcam	Ab93876	-	Rabbit	1:200
Osteonectin	ThermoFisher	MA1-43027	-	Mouse	1:500
Osteopontin	ThermoFisher	14-9096-82	-	Mouse	1:200
OSX	Abcam	ab22552	-	Rabbit	1:200
Podoplanin	Abcam	ab128994	-	Rabbit	1:200
RUNX2	Abcam	Ab23981	-	Rabbit	1:500
Sclerostin	ThermoFisher	PA5-37943	-	Goat	1:200
Goat IgG (H+L)	Jackson Immuno	A11055	Alexa 488	Donkey	1:200

Mouse IgG (H+L)	Molecular Probes	A21236	Alexa 647	Goat	1:200
Mouse IgG (H+L)	Jackson Immuno	715-545-150	Alexa 488	Donkey	1:200
Rabbit IgG (H+L)	Invitrogen	A21206	Alexa 488	Donkey	1:200
Rabbit IgG (H+L)	Molecular Probes	A21244	Alexa 647	Goat	1:200
Alizarin Red	Sigma-Aldrich	A5533	-	-	2%
Picrosirius Red	Sigma-Aldrich	365548	-	-	0.1%
Alcian blue	Sigma-Aldrich	A5268	-	-	1%

Sample preparation for electron microscopy:

Samples were processed for electron microscopy as previously described[35]. In short, co-culture samples were fixed in 2.5% glutaraldehyde and 2% paraformaldehyde in 0.1 M sodium cacodylate buffer (CB) for 72 h and washed 5 times in 0.1 M CB and 5 times in double-distilled water (ddH_2O). Co-cultures were then post fixed using 1% OsO_4 with 0.8% $K_3Fe(CN)_6$ in 0.1 M CB for 1 hour on ice. After rinsing in 0.1 M CB, the co-cultures were treated with 1% Tannic acid followed by 1% uranyl acetate in ddH_2O for 1 hour. Finally, the samples were rinsed using ddH_2O, dehydrated with ethanol (50%, 70%, 90%, 96%, 100%), and embedded in Epon resin.

Focused Ion Beam Scanning Electron Microscopy (FIB/SEM) imaging:

Epon embedded samples were imaged with a Scios FIB/SEM (Thermo Fisher Scientific, Breda, The Netherlands) under high vacuum conditions. Using the gas injection system (GIS) in the FIB/SEM microscope, a 500 nm thick layer of Pt was deposited over the ROI, at an acceleration voltage of 30 kV and a current of 1 nA. Trenches flanking the ROI were milled at an acceleration voltage of 30 kV,

304 using a high FIB beam current (5-7 nA), followed by a staircase pattern in front of the ROI to expose
305 the imaging surface. Fine polishing was performed with the ion beam set to 30 kV with a FIB beam
306 current of 0.5 nA, resulting in a smooth imaging surface. Serial imaging was then performed using the
307 in-column backscattered electron detector, and the following settings: Acceleration voltage 2 kV,
308 Beam current 0.2 nA, Pixel dwell time 10 µs, voxel size: 30x30x30 nm (stack in video 1) and 10x10x20
309 nm (stack in Video 2).
310
311 **Sample preparation for Transmission Electron Microscopy (TEM):**
312 Epon embedded samples: 70 nm sections from resin embedded blocks were made using an ultra-
313 microtome (Leica), and collected on carbon coated copper TEM grids. Post staining with uranyl
314 acetate and led citrate was performed using the Leica EM AC20 automatic contrasting instrument.
315
316 **Preparation and Immunogold labelling of Tokuyasu Sections:**
317 Thin sections were prepared following the Tokuyasu protocol[36,37]. Briefly, co-cultures were fixed as
318 described above and infiltrated overnight in 2.3 M sucrose for cryo-protection. Small blocks of the
319 co-cultures were mounted on aluminum pins and plunge frozen in liquid nitrogen. 70 nm thick
320 cryosections were sectioned with a cryo-ultramicrotome and picked up with a mixture of 2%
321 methylcellulose/2.3 M sucrose on copper support grids coated with formvar and carbon. After rinsing
322 away the pick-up solution in PBS at 37° C for 30 minutes, the sections were treated with PBS
323 containing 0.15% glycine, followed by blocking for 10 minutes with 0.5% cold fish skin gelatin and
324 0.1% BSA-c in PBS. The TEM grids were incubated for 1 hour with a collagen type 1 antibody in
325 blocking solution (Abcam, AB34710). The grids were then rinsed with 0.1% BSA in PBS and incubated
326 with 10-nm Au particles conjugated to Protein-A in blocking solution.[38] The sections were then
327 thoroughly washed in ddH_2O, stained with uranyl acetate and embedded in methylcellulose.[38]
328
329

330 **TEM imaging:**

331 The sections were imaged using a Tecnai T12 TEM (80kV) (Thermo Fisher Scientific, Breda, The
332 Netherlands), equipped with Veleta (EMSIS GmbH, Münster, Germany).

333

334 **Raman spectroscopy:**

335 Raman measurements were conducted using a WiTec Alpha 300R confocal Raman microscope. Co-
336 culture samples were fixed in 10% neutral buffered formalin (24 h at 4° C), incubated for 2 hours in
337 5% sucrose at 4° C, embedded in Tissue-Tek (Sakura Finetek 4609024), cut into 10 µm thick sections
338 and mounted on Poly-L-Lysine coated microscope slides. Raman imaging was conducted using 532
339 nm excitation lasers with a laser power of 10 mW, using 50x 0.8 objective (0.8 NA) with a grating of
340 600 gr/mm. The maps were obtained with a spatial resolution of 3 spectra/µm. Data analysis was
341 performed using Project V plus software (Witec , Ulm) and Origin 8.

342

343 **FTIR spectroscopy:**

344 Prior to the FTIR measurement, the co-culture samples were freeze dried overnight. After drying, 1.5
345 mg of the samples was crushed using mortar and pestle until a fine powder was achieved. After this,
346 148.5 mg of KBr was added to the mortar and pestle and the materials were mixed and further
347 crushed to a fine homogeneous mixture. The mixture was added to a pellet press holder, the
348 transparent and homogeneous pellets were then inserted into the FTIR spectrometer (Perking Elmer
349 one 1600). The FTIR spectra were obtained in transmission mode. Spectra were obtained over the
350 range form 200 cm^{-1} to 6000 cm^{-1} with a spectral resolution of 0.5 cm^{-1}.

351 **Image Analysis:**

352 3D FIB/SEM Image processing was performed using Matlab and Avizo 3D software (FEI VSG,
353 www.avizo3d.com). 3D image reconstruction, alignment, denoising and brightness and contrast
354 adjustments were done usign Matlab. 3D segmentation was done using Avizo. Segmentation was

355 performed using manual thresholding, and cell processes were counted manually. As all cells were
356 only partially captured in the available FIB/SEM volume, cell process density was determined per unit
357 surface area of the cell body. The surface areas of cell parts captured in the FIB/SEM volume were
358 calculated from the segmented 3D image mask using Matlab and Fiji. Further details are given in
359 Supplementary Fig. 11.
360 Cell density was determined from the number of cells in the imaged FIB/SEM volume (20 μm x 20 μm
361 x 40 μm) and compared to literature data from histological sections[19] (volume 5 μm x 1000 μm x
362 1000 μm).
363

364 **References**

365 1 Fatehullah, A., Tan, S. H. & Barker, N. Organoids as an in vitro model of human development
366 and disease. *Nat Cell Biol* **18**, 246-254, doi:10.1038/ncb3312 (2016).
367 2 in *Principles of Bone Biology (Fourth Edition)* (eds John P. Bilezikian, T. John Martin, Thomas
368 L. Clemens, & Clifford J. Rosen) 1943-1986 (Academic Press, 2020).
369 3 Owen, R. & Reilly, G. C. In vitro Models of Bone Remodelling and Associated Disorders. *Front*
370 *Bioeng Biotechnol* **6**, 134, doi:10.3389/fbioe.2018.00134 (2018).
371 4 Bonewald, L. F. The amazing osteocyte. *J Bone Miner Res* **26**, 229-238, doi:10.1002/jbmr.320
372 (2011).
373 5 Franz-Odendaal, T. A., Hall, B. K. & Witten, P. E. Buried alive: How osteoblasts become
374 osteocytes. *Dev Dynam* **235**, 176-190 (2006).
375 6 Zhang, C., Bakker, A. D., Klein-Nulend, J. & Bravenboer, N. Studies on Osteocytes in Their 3D
376 Native Matrix Versus 2D In Vitro Models. *Curr Osteoporos Rep* **17**, 207-216,
377 doi:10.1007/s11914-019-00521-1 (2019).
378 7 Wang, K. *et al.* A Novel Osteogenic Cell Line That Differentiates Into GFP-Tagged Osteocytes
379 and Forms Mineral With a Bone-Like Lacunocanalicular Structure. *J Bone Miner Res* **34**, 979-
380 995, doi:10.1002/jbmr.3720 (2019).
381 8 Iordachescu, A. *et al.* An In Vitro Model for the Development of Mature Bone Containing an
382 Osteocyte Network. *Advanced Biosystems* **2**, doi:10.1002/adbi.201700156 (2018).
383 9 Thrivikraman, G. *et al.* Rapid fabrication of vascularized and innervated cell-laden bone models
384 with biomimetic intrafibrillar collagen mineralization. *Nat Commun* **10**, 3520,
385 doi:10.1038/s41467-019-11455-8 (2019).
386 10 Nasello, G. *et al.* Primary Human Osteoblasts Cultured in a 3D Microenvironment Create a
387 Unique Representative Model of Their Differentiation Into Osteocytes. *Frontiers in*
388 *Bioengineering and Biotechnology* **8**, doi:10.3389/fbioe.2020.00336 (2020).
389 11 Skottke, J., Gelinsky, M. & Bernhardt, A. In Vitro Co-culture Model of Primary Human
390 Osteoblasts and Osteocytes in Collagen Gels. *Int J Mol Sci* **20**, doi:10.3390/ijms20081998
391 (2019).
392 12 Vetsch, J. R., Paulsen, S. J., Muller, R. & Hofmann, S. Effect of fetal bovine serum on
393 mineralization in silk fibroin scaffolds. *Acta Biomater* **13**, 277-285,
394 doi:10.1016/j.actbio.2014.11.025 (2015).
395 13 Melke, J., Zhao, F., van Rietbergen, B., Ito, K. & Hofmann, S. Localisation of mineralised tissue
396 in a complex spinner flask environment correlates with predicted wall shear stress level
397 localisation. *Eur Cell Mater* **36**, 57-68, doi:10.22203/eCM.v036a05 (2018).
398 14 Kerschnitzki, M. *et al.* Bone mineralization pathways during the rapid growth of embryonic
399 chicken long bones. *J Struct Biol* **195**, 82-92, doi:10.1016/j.jsb.2016.04.011 (2016).
400 15 Kenneth E. S. Poole, R. L. v. B., Nigel Loveridge, Herman Hamersma, & Socrates E. Papapoulos,
401 C. W. L., and Jonathan Reeve. Sclerostin is a delayed secreted product of osteocytes that
402 inhibits bone formation. *The FASEB Journal* **19**, 1842-1844 (2005).
403 16 Verbruggen, S. W., Vaughan, T. J. & McNamara, L. M. Strain amplification in bone
404 mechanobiology: a computational investigation of the in vivo mechanics of osteocytes. *J R Soc*
405 *Interface* **9**, 2735-2744, doi:10.1098/rsif.2012.0286 (2012).
406 17 Varga, P. *et al.* Synchrotron X-ray phase nano-tomography-based analysis of the lacunar-
407 canalicular network morphology and its relation to the strains experienced by osteocytes in
408 situ as predicted by case-specific finite element analysis. *Biomech Model Mechanobiol* **14**, 267-
409 282, doi:10.1007/s10237-014-0601-9 (2015).
410 18 Kerschnitzki, M. *et al.* The organization of the osteocyte network mirrors the extracellular
411 matrix orientation in bone. *J Struct Biol* **173**, 303-311, doi:10.1016/j.jsb.2010.11.014 (2011).
412 19 Yair, R., Cahaner, A., Uni, Z. & Shahar, R. Maternal and genetic effects on broiler bone
413 properties during incubation period. *Poult Sci* **96**, 2301-2311, doi:10.3382/ps/pex021 (2017).
414 20 Tokarz, D. *et al.* Intravital imaging of osteocytes in mouse calvaria using third harmonic
415 generation microscopy. *PLoS One* **12**, e0186846, doi:10.1371/journal.pone.0186846 (2017).

21 and, S. W. & Wagner, H. D. THE MATERIAL BONE: Structure-Mechanical Function Relations. *Annual Review of Materials Science* **28**, 271-298, doi:10.1146/annurev.matsci.28.1.271 (1998).

22 Reznikov, N., Shahar, R. & Weiner, S. Three-dimensional structure of human lamellar bone: The presence of two different materials and new insights into the hierarchical organization. *Bone* **59**, 93-104, doi:https://doi.org/10.1016/j.bone.2013.10.023 (2014).

23 Reznikov, N., Shahar, R. & Weiner, S. Bone hierarchical structure in three dimensions. *Acta Biomaterialia* **10**, 3815-3826 (2014).

24 de Wildt, B. W. M. *et al.* From bone regeneration to three-dimensional in vitro models: tissue engineering of organized bone extracellular matrix. *Current Opinion in Biomedical Engineering* **10**, 107-115, doi:https://doi.org/10.1016/j.cobme.2019.05.005 (2019).

25 Kazanci, M., Roschger, P., Paschalis, E. P., Klaushofer, K. & Fratzl, P. Bone osteonal tissues by Raman spectral mapping: Orientation–composition. *Journal of Structural Biology* **156**, 489-496, doi:https://doi.org/10.1016/j.jsb.2006.06.011 (2006).

26 Akiva, A. *et al.* Mineral Formation in the Larval Zebrafish Tail Bone Occurs via an Acidic Disordered Calcium Phosphate Phase. *J Am Chem Soc* **138**, 14481-14487, doi:10.1021/jacs.6b09442 (2016).

27 McKee, M. D. & Nanci, A. Postembedding colloidal-gold immunocytochemistry of noncollagenous extracellular matrix proteins in mineralized tissues. *Microscopy Research and Technique* **31**, 44-62, doi:10.1002/jemt.1070310105 (1995).

28 Weiner, S. & Traub, W. Organization of hydroxyapatite crystals within collagen fibrils. *FEBS letters* **206**, 262-266 (1986).

29 Park, S. E., Georgescu, A. & Huh, D. Organoids-on-a-chip. *Science* **364**, 960-965, doi:10.1126/science.aaw7894 (2019).

30 Hofmann, S. *et al.* Control of in vitro tissue-engineered bone-like structures using human mesenchymal stem cells and porous silk scaffolds. *Biomaterials* **28**, 1152-1162, doi:10.1016/j.biomaterials.2006.10.019 (2007).

31 Nazarov, R., Jin, H.-J. & Kaplan, D. L. Porous 3-D Scaffolds from Regenerated Silk Fibroin. *Biomacromolecules* **5**, 718-726, doi:10.1021/bm034327e (2004).

32 Hildebrand T, L. A., Muller R, Dequeker J, Ruegsegger P. Direct three-dimensional morphometric analysis of human cancellous bone: microstructural data from spine, femur, iliac crest, and calcaneus. *J. Bone Miner. Res.* **14** (1999).

33 van Lenthe, G. H. *et al.* Nondestructive micro-computed tomography for biological imaging and quantification of scaffold-bone interaction in vivo. *Biomaterials* **28**, 2479-2490, doi:10.1016/j.biomaterials.2007.01.017 (2007).

34 Krahn, K. N., Bouten, C. V. C., van Tuijl, S., van Zandvoort, M. A. M. J. & Merkx, M. Fluorescently labeled collagen binding proteins allow specific visualization of collagen in tissues and live cell culture. *Analytical Biochemistry* **350**, 177-185, doi:https://doi.org/10.1016/j.ab.2006.01.013 (2006).

35 Fermie, J. *et al.* Single organelle dynamics linked to 3D structure by correlative live-cell imaging and 3D electron microscopy. *Traffic* **19**, 354-369, doi:10.1111/tra.12557 (2018).

36 Oorschot VMJ, S. T., Bryson-Richardson RJ, Ramm G. . in *Correl. Light Electron Microsc. II* 241-258 (Academic Press, 2014).

37 van Meel, E. *et al.* Disruption of the Man-6-P targeting pathway in mice impairs osteoclast secretory lysosome biogenesis. *Traffic* **12**, 912-924, doi:10.1111/j.1600-0854.2011.01203.x (2011).

38 Slot, J., Geuze, H. Cryosectioning and immunolabeling. *Nat protoc* **2**, 2480-2491, doi:https://doi.org/10.1038/nprot.2007.365 (2007).

39 Nyman, J. S. *et al.* Measuring Differences in Compositional Properties of Bone Tissue by Confocal Raman Spectroscopy. *Calcified Tissue International* **89**, 111-122, doi:10.1007/s00223-011-9497-x (2011).

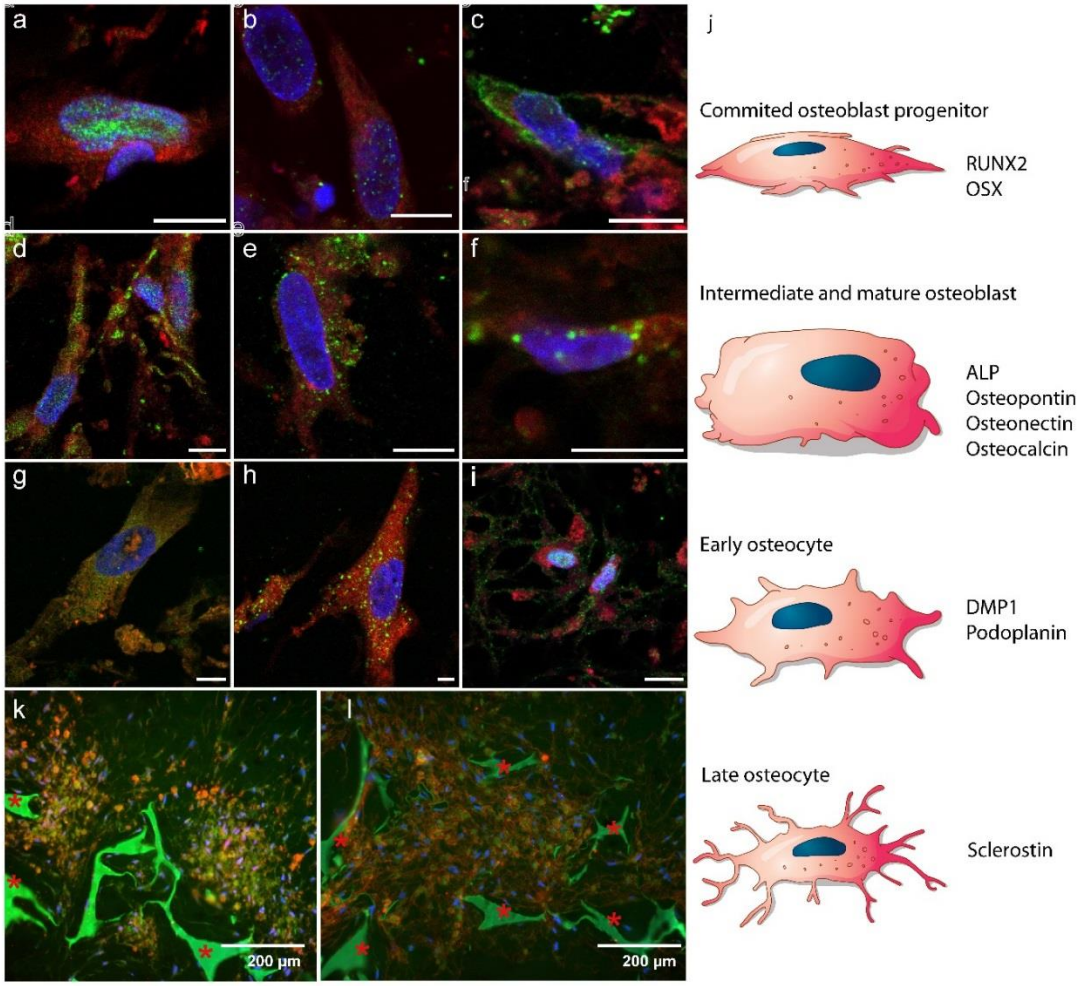

Figure 1: Differentiation of hBMSCs into osteoblasts and osteocytes: a-i) Fluorescence immunohistochemistry imaging showing markers for a-c) early stages of osteoblast formation, d-f) mature osteoblasts, and g-i) osteocyte development (5.6 mM glucose). Color code: red - cell cytoplasm, blue - cell nuclei, green: a) RUNX2 (day 7) , b) OSX (day 7), c) ALP (day 26), d) osteocalcin (day 26), e) osteopontin (day 26), f) osteonectin (day 21), g) DMP1 (day 28), h) podoplanin (day 28), i) sclerostin (day 28). Scale bars: 10 µm. See Supplementary Fig.4 for separate channels. j) Schematic illustration of MSC differentiation into osteoblasts and osteocytes, indicating at which state which protein expression is expected in a-i. k,l) Fluorescent images indicating self-organized domains of osteocytes embedded in a mineralized matrix after 8 weeks (25 mM glucose), k) co-localization of osteocytes (sclerostin, red) and mineral (calcein, green) and l) collagen (CNA35, red) and mineral (calcein, green) * Indicates the silk fibroin scaffold.

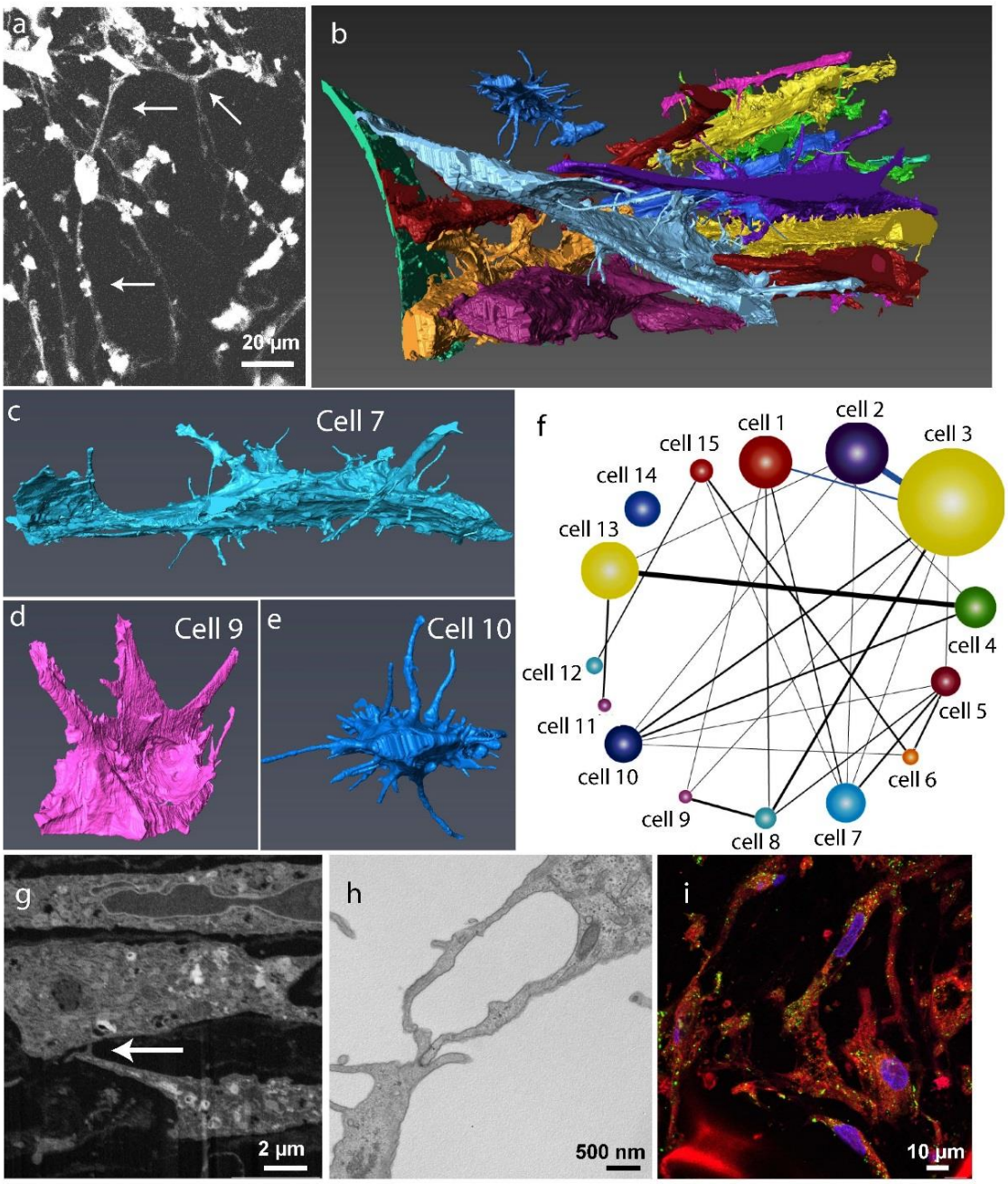

480

481 **Figure 2: Osteocyte development and network formation.** a) Fluorescent cytoplasm staining

482 showing the development of long (> 5µm, arrows) cell processes connecting cells, and the formation

483 of an interconnected network. The long processes were enhanced using a gamma value of -1.5. (see

484 original image in supplementary fig. 6). b) 3D FIB/SEM reconstruction showing cell morphology and

485 network formation in the whole volume. c-e) Details from the 3D reconstruction in (b) showing

486 individual osteocytes in different stages of morphological development (cell numbers refer to

identification in supplementary Fig. 7). c) Cell #7, d) cell #9, e) cell #14. f-i) Cell connectivity: f) Connectivity map of the cells in the 3D FIB/SEM stack (see also Supplementary Tables 1 and 2). Sizes of the circles reflect the number of processes of that respective cell. Thickness of the lines reflects the number of connections between individual cells (cell numbers refer to identification in supplementary Fig. 7). g) single slice from the 3D FIB/SEM stack showing long processes (arrow), creating a cellular network. h) TEM image shows a gap junction between processes of two connecting cells. i) fluorescent immunohistochemistry showing the presence of gap junctions on the surface of the different cells. Color code: red - cell cytoplasm, blue - cell nuclei, green - connexin43.

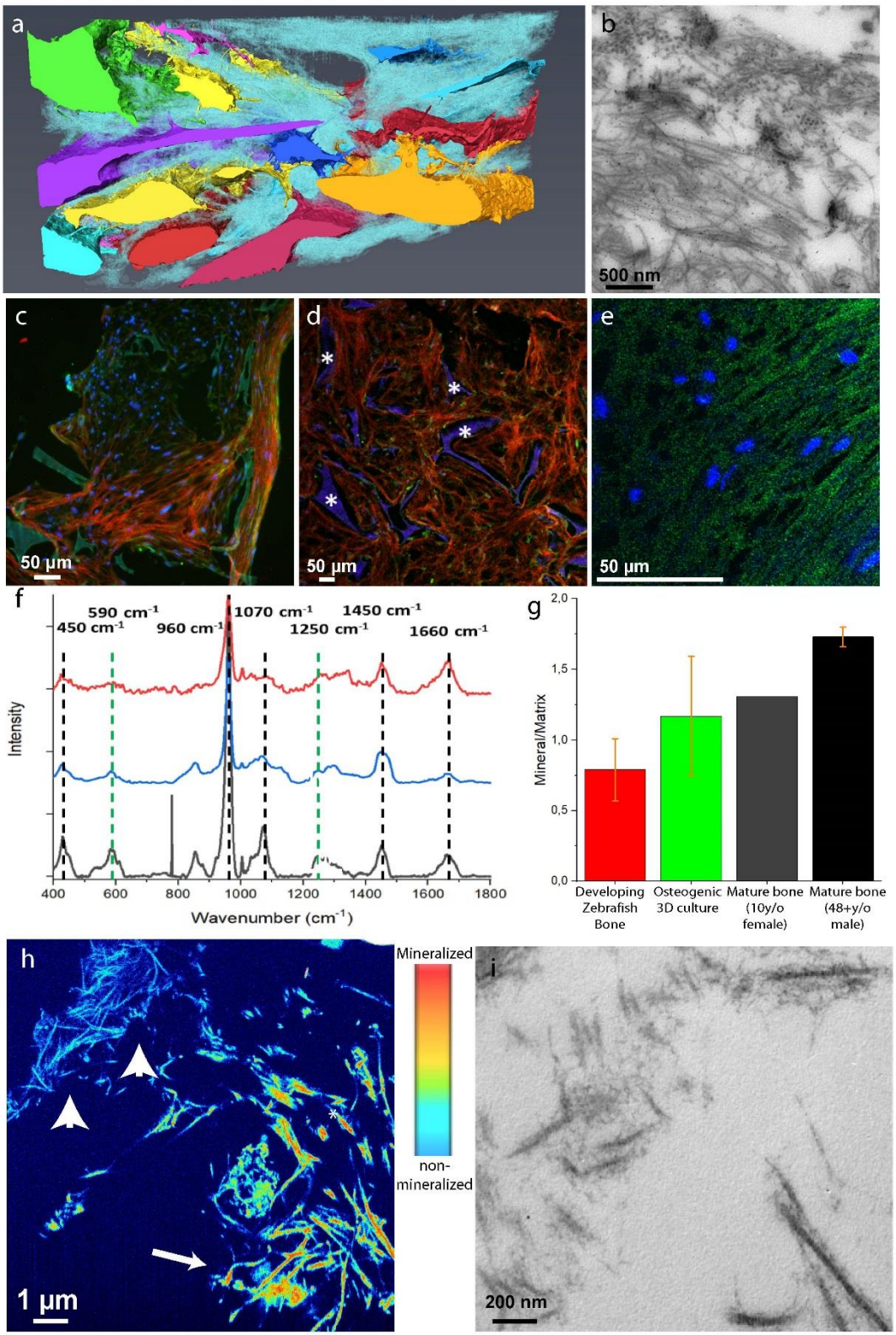
a
b
500 nm
c
50 µm
d
50 µm
e
50 µm
f
590 cm-1
450 cm-1
960 cm-1
1070 cm-1
1450 cm-1
1250 cm-1
1660 cm-1
Intensity
400
600
800
1000
1200
1400
1600
1800
Wavenumber (cm-1)
g
Mineral/Matrix
2,0
1,5
1,0
0,5
0,0
Developing Zebrafish Bone
Osteogenic 3D culture
Mature bone (10y/o female)
Mature bone (48+y/o male)
h
1 µm
Mineralized
non-mineralized
i
200 nm

495

496

497

498 **Figure 3: Extracellular matrix development:** a) 3D FIB/SEM reconstruction shows the embedding of
499 the cells in the collagen matrix (cyan). Discrete cells are represented with different colors. b) TEM
500 image of a 70 nm section showing the random distribution of collagen fibrils. Collagen type I was
501 identified by immunolabelling. c-e) Fluorescent immunohistochemistry identifying key non-
502 collagenous proteins in the collagenous matrix: c) Co-localization of osteocalcin (green) and collagen
503 (red). d) Osteopontin (green) distribution in the collagen matrix (red). * Indicates the silk fibroin
504 scaffold. e) Co-localization of DMP1 (green) with the collagen structure (see supplementary Fig. 5 for
505 collagen image). f-g) Raman microspectrometry of mineralized matrices. f) Localized Raman spectra
506 of mineralized collagen of developing zebrafish bone (red), the 3D osteogenic co-culture (blue) and
507 human bone of a 10 year old female (grey g) Raman derived mineral/matrix ratios of 4 mineralized
508 tissues of zebrafish (N=6, red), Osteogenic 3D culture (N=7, green), 10 year old human female (N=1,
509 grey), and 48+ years old human male (N=7, black, taken from reference[39]). Bars indicate sample
510 standard deviations. h) Heat map presentation of a 3D FIB/SEM cross section showing collagen fibrils
511 with different degrees of mineralization (see Supplementary Fig. 10). Arrowheads indicate non-
512 mineralized collagen fibrils (light blue), arrow indicates mineralized collagen fibril (orange) i) TEM
513 image showing individual mineralized collagen fibrils.